JOURNAL OF SCIENCE TECHNOLOGY AND EDUCATION 14(3), OCTOBER, 2026
E-ISSN: 3093-0898, PRINT ISSN: 2277-0011; Journal homepage: www.atbufstejoste.com

Spatial Grading of Critical Current Density and Temperature-Dependent Magnetic Hysteresis in a Model Superconducting Slab

Naziha Nassar Aneizan
General Directorate of Education Salahaddin, Ministry of Education, Iraq

ABSTRACT

An isothermal one-dimensional Bean model is used to compare magnetic shielding and hysteretic loss for uniform, surface-enhanced and core-enhanced critical-current profiles with identical spatial means. A prescribed thermal factor, $f(t) = (1 - t^2)^2$ with $t = T/T_c$, scales the current density without fitting a specific material. Applied induction is normalized by a fixed reference induction; loop area is the positive area enclosed by dimensionless magnetization against normalized field. Signed field-history updates generate closed magnetization loops for 27 combinations of temperature, field amplitude and grading. At $t = 0.30$ and peak normalized field $H = 0.50$, surface enhancement reduces loop area by 34.1% relative to core enhancement; at $H = 1.50$, it increases area by 33.9%. An independent cycle integral reproduces the numerical areas to within 5.25×10^{-6}. An analytical expression establishes an exact crossing at $H = f(t)$ for the opposite linear gradings considered here. Full results, convergence checks and executable source code are supplied. The comparison identifies how redistributing a fixed mean critical-current capacity changes shielding and loss within this idealized, dimensionless model. It does not provide experimentally calibrated predictions for a named superconductor.

ARTICLE INFO
Article History
Received: October, 2026
Received in revised form: October, 2026
Accepted: October, 2026
Published online: October, 2026

KEYWORDS
Bean Model; Graded Critical Current; Magnetic Hysteresis; Flux Penetration; Numerical Verification.

INTRODUCTION

Bean's critical-state model describes magnetic history in a type-II superconductor by restricting the current density associated with irreversible flux penetration (Bean, 1962, 1964). Vortex pinning provides the physical context for this macroscopic description (Campbell & Evetts, 1972). Field-dependent critical current, flux creep and finite geometry require extensions beyond the simplest Bean slab (Kim et al., 1963; Brandt, 1995, 1996).

The spatial allocation of critical current can matter even when its volume average is unchanged. Zhao and Zhou (2011) numerically studied a slab divided into regions with different critical-current densities using a flux-creep formulation and reported changes in complex AC susceptibility. Their work already establishes that current-density inhomogeneity affects magnetic response. The question examined here is narrower: how do opposite, continuous linear profiles with equal means change closed-cycle loop area as field amplitude crosses the common virgin full-penetration field?

Analytical loss calculations and thin-strip solutions demonstrate the importance of specifying excitation and geometry (Norris, 1970; Brandt & Indenbom, 1993; Zeldov et al., 1994). AC susceptibility and computational reviews provide broader context for magnetic screening and loss calculations (Gömöry, 1997; Grilli et al., 2014; Ainslie & Fujishiro, 2015). Three-dimensional and H-formulation methods address configurations outside the present one-dimensional model (Zhang & Coombs, 2012; Shen et al., 2020).

This study compares uniform, surface-enhanced and core-enhanced profiles under identical spatial means and isothermal field histories. A phenomenological temperature factor is prescribed rather than inferred from

Corresponding author: Naziha Nassar Aneizan
nazehanassar5@gmail.com
General Directorate of Education Salahaddin, Ministry of Education, Iraq.
© 2026. Faculty of Technology Education. ATBU Bauchi. All rights reserved

JOURNAL OF SCIENCE TECHNOLOGY AND EDUCATION 14(3), OCTOBER, 2026
E-ISSN: 3093-0898, PRINT ISSN: 2277-0011; Journal homepage: www.atbufstejoste.com

experimental data; alternative temperature laws are known to give different responses (Hong et al., 2019). The contribution is a controlled comparison of field-dependent loss ordering for this profile family, supported by an exact cycle integral and explicit numerical verification. No claim is made that spatial inhomogeneity itself is new.

MATHEMATICAL MODEL AND COMPUTATIONAL METHOD

Geometry and definitions

Consider an infinite slab of thickness $2a$ with applied induction B_a parallel to its wide faces. On the symmetric half slab, $u = x/a$ runs from the centre $(u = 0)$ to the surface $(u = 1)$. Let J_{ref} be a fixed reference current density and μ_0 the vacuum permeability. Define

$$B_{ref} = \mu_0 J_{ref} a, \qquad h = \frac{B_a}{B_{ref}}, \qquad b = \frac{B}{B_{ref}}. \qquad (1)$$

Using Equation (1), the dimensionless magnetization is $m = \mu_0 M/B_{ref} = \int_0^1 b\,(u)\,du - h$, where B is the internal induction and M is the volume magnetization. Demagnetizing fields, reversible magnetization and flux creep are excluded. The field-gradient constraint is $|\,\partial b/\,\partial u| \le q$, where $q = J_c/J_{ref}$.

Spatial and thermal profiles

At fixed reduced temperature $t = T/T_c$, where T_c is the model critical temperature, prescribe

$$q(u,t) = f(t)[1 + g(2u-1)], f(t) = (1-t^2)^2 \quad (2)$$

In Equation (2), $0 \le t < 1$ and $g \in \{-0.60, 0, +0.60\}$. Negative g strengthens the core, positive g strengthens the surface, and zero g is uniform. Since $\int_0^1 (2u-1)\,du = 0$, all profiles have mean $f(t)$; $|g| < 1$ keeps q positive. The exponent two is illustrative and is not a universal material law (Hong et al., 2019). The cumulative shielding is

$$S(u,t) = \int_u^1 q\,(s,t)\,ds = f(t)[(1-u) + gu(1-u)]. \qquad (3)$$

Equation (3) gives $S(1,t) = 0$ and the virgin full-penetration field $h_p = S(0,t) = f(t)$ for all three profiles.

Signed field updates and cycle construction

Let b_i^k be the induction at node u_i after signed applied field h_k. Starting from zero-field cooling, $h_0 = 0$ and $b_i^0 = 0$. A monotone increase uses

$$b_i^{k+1} = \max\{b_i^k,\ h_{k+1} - S(u_i,t)\}, \quad h_{k+1} \ge h_k. (4)$$

A monotone decrease uses

$$b_i^{k+1} = \min\{b_i^k,\ h_{k+1} + S(u_i,t)\}, \quad h_{k+1} \le h_k. \quad (5)$$

Equations (4) and (5) retain the previous state b_i^k and its reversal history. Negative applied and internal fields are retained with their signs; no absolute-field substitution is used. At the surface both updates impose $b(1) = h$. Each run follows $0 \to +H \to -H \to +H$, where $H = h_{max} > 0$. The initial ramp gives $b = \max(0, h - S)$. The descending and final ascending branches form the reported closed cycle. Equality of the first and final states at $+H$ is checked explicitly.

Loop area and an independent cycle integral

Let $m_{down}(h)$ and $m_{up}(h)$ denote magnetization on the descending and ascending branches. Their positive enclosed area is

$$A = \int_{-H}^{H} [m_{down}(h) - m_{up}(h)]\ dh. \qquad (6)$$

Within this quasistatic infinite-slab model, volumetric energy loss per cycle is $Q = (B_{ref}^2/\mu_0)A$. Only A is reported because B_{ref} is not calibrated. The quantity is a magnetic loop area, not resistivity, measured power or an experimental observation.

An independent integral follows by evaluating the local branch difference. A position with $S > H$ remains unchanged throughout the cycle. For $S \le H$, the two switching fields are $h = H - 2S$ and $h = -H + 2S$; integrating the local branch difference gives $4S(H - S)$. Interchanging the spatial and field integrals yields

$$A = 4\int_{u_f}^{1} S\,(u,t)[H - S(u,t)]\,du. \qquad (7)$$

Corresponding author: Naziha Nassar Aneizan
nazehanassar5@gmail.com
General Directorate of Education Salahaddin, Ministry of Education, Iraq.
© 2026. Faculty of Technology Education. ATBU Bauchi. All rights reserved

JOURNAL OF SCIENCE TECHNOLOGY AND EDUCATION 14(3), OCTOBER, 2026
E-ISSN: 3093-0898, PRINT ISSN: 2277-0011; Journal homepage: www.atbufstejoste.com

Here u_f is the unique solution of $S(u_f, t) = H$ for $0 < H < f(t)$, and $u_f = 0$ for $H \geq f(t)$.

Equation (7) is evaluated independently of the update algorithm. Its integrand is a polynomial of degree at most four, so three-point Gauss-Legendre quadrature is exact apart from floating-point roundoff.

For full penetration, direct integration gives, with $f = f(t)$,

$$A_g = 2fH - \frac{4f^2}{3} + \frac{2gf(H-f)}{3} - \frac{2g^2f^2}{15}, \quad H \geq f. \quad (8)$$

For opposite gradings $g = \pm\gamma$, where $0 < \gamma < 1$,

$$A_{+\gamma} - A_{-\gamma} = \frac{4\gamma f(H-f)}{3}, \quad H \geq f. \quad (9)$$

Equation (9) establishes an exact crossing at $H = f(t)$, and positive surface-minus-core area above that field. Below it, Equation (7) is used rather than extrapolating Equation (8). The numerical sweep verifies the lower surface-enhanced area in that regime. The exact crossing relies on these opposite linear profiles and the stated Bean assumptions.

Computational matrix and reproducibility

All three profiles are computed at all three temperatures and field amplitudes: nine temperature-field combinations and 27 individual cases (Table 1). The half slab uses 801 equally spaced nodes. Field grids include both endpoints exactly and have maximum increment 0.005. Magnetization and Equation (6) use composite trapezoidal quadrature. Independent benchmarks, closure, boundary and slope checks are performed. The supplied implementation was run with Python 3.12.14, NumPy 2.3.5 and Matplotlib 3.10.8.

Table 1. Complete nondimensional simulation matrix.

Parameter	Values or definition
Geometry	Infinite slab; $0 \leq u \leq 1$
Reduced temperature *t*	0.30, 0.60, 0.80; separate isothermal runs
Grading *g*	−0.60, 0, +0.60
Peak field *H*	0.50, 1.00, 1.50
Thermal scale	$f(t) = (1-t^2)^2$
Spatial and field resolution	801 nodes; maximum field increment 0.005

RESULTS

Virgin shielding and penetration

Figure 1 compares the equal-mean profiles and virgin induction. For a positive virgin field $h < f(t)$, the front satisfies $S(u_f, t) = h$; $u_f = 0$ at or above full penetration. At $t = 0.30$, $f = 0.8281$. At $h = 0.50$, the front positions are $u_f = 0.2762$, 0.3962 and 0.5450 for core-enhanced, uniform and surface-enhanced current, respectively. The virgin flux-free core occupies $0 \leq u \leq u_f$; larger u_f therefore means shallower penetration. Although the front locations differ, their full-penetration field remains identical.

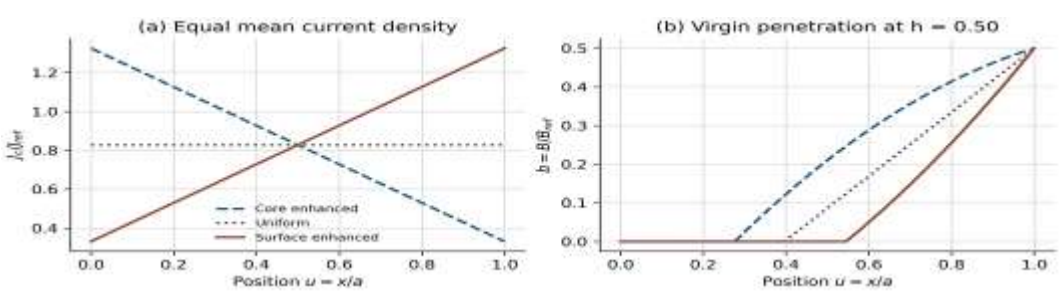

Figure 1. Equal-mean critical-current profiles (a) and virgin induction at t = 0.30 and h = 0.50 (b). The coordinate runs from centre to surface. All axes are dimensionless.

Corresponding author: Naziha Nassar Aneizan
nazehanassar5@gmail.com
General Directorate of Education Salahaddin, Ministry of Education, Iraq.
© 2026. Faculty of Technology Education. ATBU Bauchi. All rights reserved

JOURNAL OF SCIENCE TECHNOLOGY AND EDUCATION 14(3), OCTOBER, 2026
E-ISSN: 3093-0898, PRINT ISSN: 2277-0011; Journal homepage: www.atbufstejoste.com

Closed magnetization loops

Figure 2 shows both cycle branches at $H = 1.50$. At $t = 0.30$, surface enhancement gives the largest area. At $t = 0.80$, all areas decrease because the prescribed current scale is smaller. These are closed magnetic cycles under constant temperature, distinct from the virgin shielding response in Figure 1.

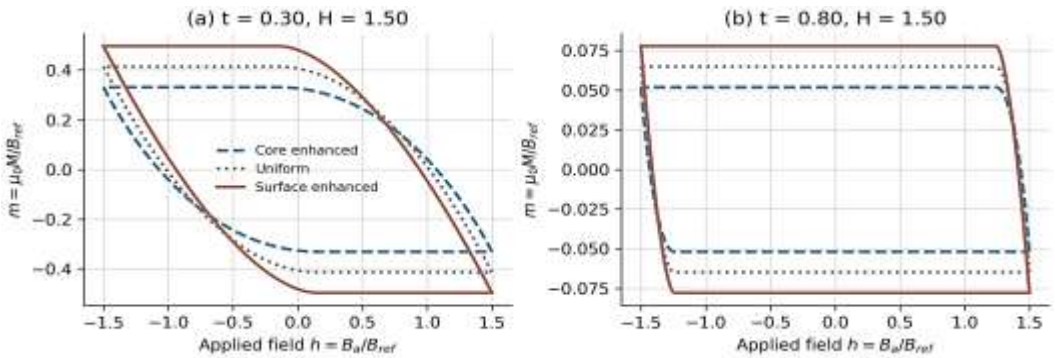

Figure 2. Descending and ascending magnetization branches at H = 1.50 for t = 0.30 (a) and 0.80 (b). Line styles identify the same profiles in both panels.

Complete area results and field-dependent ordering

Table 2 reports every announced temperature-field combination. At $t = 0.30$ and $H = 0.50$, surface enhancement lowers area from 0.114085 to 0.075190, a 34.1% reduction relative to core enhancement. At $H = 1.50$, it raises area from 1.314487 to 1.759606, a 33.9% increase. At higher temperatures all three chosen field amplitudes exceed $f(t)$, so surface enhancement gives the larger area throughout those rows.

Table 2. Complete numerical loop areas from Equation (6). All values are dimensionless simulations; entries are rounded to six decimals.

t	H	Core $g = -0.6$	Uniform $g = 0$	Surface $g = +0.6$
0.30	0.50	0.114085	0.100629	0.075190
0.30	1.00	0.652006	0.741862	0.765886
0.30	1.50	1.314487	1.569962	1.759606
0.60	0.50	0.163035	0.185899	0.192657
0.60	1.00	0.490715	0.595499	0.684177
0.60	1.50	0.818396	1.005099	1.175697
0.80	0.50	0.087193	0.107201	0.125596
0.80	1.00	0.190873	0.236801	0.281116
0.80	1.50	0.294553	0.366401	0.436636

The exact crossing from Equation (9) is $H = 0.8281$ at $t = 0.30$, rather than an unexplained coincidence from a coarse scan. Bisection of the numerical surface-minus-core area brackets the root between $0.95f$ and $1.05f$ and stops at interval width below 10^{-10}. Across all three temperatures and additional resolutions of 401 nodes with field increment 0.01 and 1601 nodes with increment 0.0025, the maximum root error relative to $f(t)$ is 4.83×10^{-11}. This root-search tolerance does not represent uncertainty in a real material.

Corresponding author: Naziha Nassar Aneizan
nazehanassar5@gmail.com
General Directorate of Education Salahaddin, Ministry of Education, Iraq.
© 2026. Faculty of Technology Education. ATBU Bauchi. All rights reserved

JOURNAL OF SCIENCE TECHNOLOGY AND EDUCATION 14(3), OCTOBER, 2026
E-ISSN: 3093-0898, PRINT ISSN: 2277-0011; Journal homepage: www.atbufstejoste.com

Field and temperature sweeps

Figure 3 uses Equation (7) for dense sweeps, with the field-history calculation independently checked as described in Section 4. At weak excitation, surface enhancement reduces penetration and cycle area. At higher excitation, it increases area. At fixed $H = 1$, every plotted temperature gives full penetration at the field peak because $f(t) \leq 1$. The non-monotonic temperature dependence follows from the competing linear and negative quadratic terms in $f(t)$ in Equation (8). As the prescribed current scale approaches zero, the magnetization width and cycle area vanish.

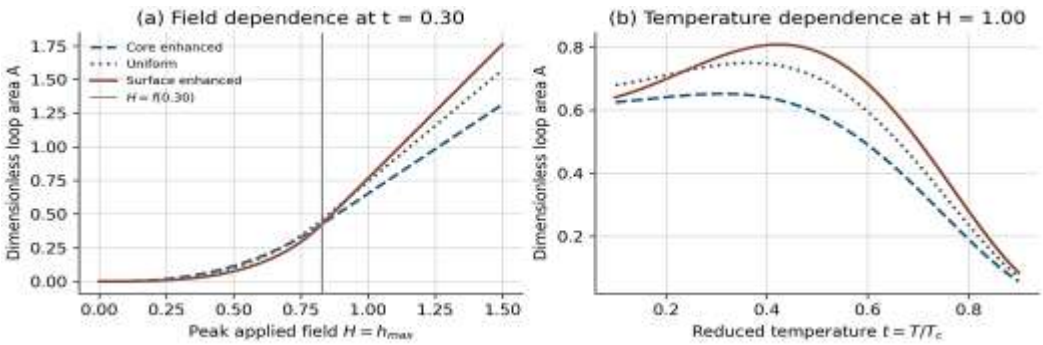

Figure 3. Dimensionless area versus peak field at t = 0.30 (a) and reduced temperature at H = 1.00 (b). Curves use the independent cycle integral. The vertical line marks the crossing of the opposite graded profiles at H = f(0.30) = 0.8281.

VERIFICATION AND DISCUSSION

Analytical and numerical checks

For the uniform virgin state and $0 \leq h \leq f$, the analytical magnetization is $m = -h + h^2/(2f)$. At $t = 0.30$ and $h = 0.25$, the absolute numerical error is 1.62×10^{-7}. For the uniform closed cycle, Equation (7) gives

$$A_0 = \frac{2H^3}{3f} \ (0 \leq H \leq f), \qquad A_0 = 2fH - \frac{4f^2}{3} \ (H \geq f). \qquad (10)$$

All nine uniform cases agree with Equation (10) to within 4.89×10^{-6}. Across all 27 graded and uniform cases, the largest error relative to Equation (7) is 5.25×10^{-6}. A separate 60-digit antiderivative evaluation and an electric-field/current work integral provide additional checks in the supplementary audit. First and final field states coincide to floating-point precision; surface boundary error is zero and the largest discrete slope excess is 2.42×10^{-13}. These are implementation checks, not experimental validation.

Table 3. Convergence of the surface-enhanced area at $t = 0.30$, $H = 1.50$. The exact cycle integral gives 1.759611361.

Spatial nodes	Maximum field increment	Numerical area
101	0.0050	1.759539510
201	0.0050	1.759590397
401	0.0050	1.759603022
801	0.0050	1.759606115
1601	0.0050	1.759606937
801	0.0200	1.759543412
801	0.0100	1.759593603
801	0.0025	1.759609243

Corresponding author: Naziha Nassar Aneizan
nazehanassar5@gmail.com
General Directorate of Education Salahaddin, Ministry of Education, Iraq.
© 2026. Faculty of Technology Education. ATBU Bauchi. All rights reserved

Table 3 separates spatial and applied-field refinement. The finest field-step pair changes area by about 3.13×10^{-6}. Six decimal places in Table 2 identify reproducible numerical outputs, not six-place physical accuracy. No stochastic error bars are assigned because the calculation has no sampling noise; discretization error is reported explicitly. Uncertainty from model choice remains and is not quantified by these numerical checks.

Interpretation and scope

Virgin shielding, full penetration and closed-cycle loss describe different aspects of the response. Moving a fixed mean critical-current capacity toward the surface preserves a larger flux-free core during the virgin ramp. Over a full cycle, however, current reversal weights different spatial regions, so stronger surface shielding does not imply smaller high-amplitude loss. Equation (9) states this distinction quantitatively for the selected linear profiles.

The reversal also occurs at smaller grading magnitude: at $t = 0.30$, profiles $g = -0.30, 0, +0.30$ give areas 0.110570, 0.100629 and 0.087831 at $H = 0.50$, and 1.450453, 1.569962 and 1.673013 at $H = 1.50$. This sensitivity check remains within the same profile family. Unlike Zhao and Zhou's (2011) piecewise non-uniform slab with flux creep, the present comparison fixes the mean current, uses continuous opposite linear gradings and evaluates rate-independent closed-cycle areas. It does not establish a universal rule for inhomogeneous superconductors.

Finite geometry, nonlinear creep and more general electromagnetic formulations can change the response (Brandt, 1996; Gurevich & Brandt, 1997; Prigozhin, 1996; Shen et al., 2020). The present model excludes anisotropy, field-dependent critical current, grain connectivity, induced heating and thermomagnetic instability. Each temperature is a separate isothermal calculation, not a heating transient. Practical predictions require measured constitutive laws and geometry-specific validation; the selected thermal scaling is illustrative (Hong et al., 2019).

CONCLUSION

Equal-mean linear current profiles produce different virgin penetration depths and magnetic loop areas in an isothermal Bean slab. At $t = 0.30$, surface enhancement reduces area by 34.1% relative to core enhancement at $H = 0.50$ and increases it by 33.9% at $H = 1.50$. An independent cycle integral verifies all 27 numerical cases, and an analytical expression establishes an exact crossing at the common penetration field $H = f(t)$ for the opposite linear profiles. The result distinguishes improved virgin shielding from reduced closed-cycle loss under explicitly stated assumptions. Its significance is a reproducible comparison within a dimensionless one-dimensional model; it does not establish quantitative performance for an experimentally characterized material.

Data and Code Availability

The accompanying archive contains simulation.py, requirements.txt, a README with execution instructions, all 27 area results, complete loop data, profile and sweep data, convergence tables, crossover scans and numerical root brackets. verification_report.json records parameters, tested software versions and numerical checks. Running python simulation.py --output results regenerates the tables and figures; python audit_checks.py --results results produces the additional high-precision and work-integral checks in additional_audit.json. Figures 1–3 use the corresponding CSV outputs; supplementary Figure S1 compares the numerical and independent crossover calculations. No experimental dataset is used or generated.

REFERENCES

Ainslie, M. D., & Fujishiro, H. (2015). Modelling of bulk superconductor magnetization. *Superconductor Science and Technology*, *28*(5), Article 053002. https://doi.org/10.1088/0953-2048/28/5/053002

Bean, C. P. (1962). Magnetization of hard superconductors. *Physical Review Letters*, *8*(6), 250–253. https://doi.org/10.1103/PhysRevLett.8.250

Corresponding author: Naziha Nassar Aneizan
nazehanassar5@gmail.com
General Directorate of Education Salahaddin, Ministry of Education, Iraq.
© 2026. Faculty of Technology Education. ATBU Bauchi. All rights reserved

Bean, C. P. (1964). Magnetization of high-field superconductors. *Reviews of Modern Physics*, *36*(1), 31–39. https://doi.org/10.1103/RevModPhys.36.31

Brandt, E. H. (1995). Electric field in superconductors with rectangular cross section. *Physical Review B*, *52*(21), 15442–15457. https://doi.org/10.1103/PhysRevB.52.15442

Brandt, E. H. (1996). Superconductors of finite thickness in a perpendicular magnetic field: Strips and slabs. *Physical Review B*, *54*(6), 4246–4264. https://doi.org/10.1103/PhysRevB.54.4246

Brandt, E. H., & Indenbom, M. (1993). Type-II-superconductor strip with current in a perpendicular magnetic field. *Physical Review B*, *48*(17), 12893–12906. https://doi.org/10.1103/PhysRevB.48.12893

Campbell, A. M., & Evetts, J. E. (1972). Flux vortices and transport currents in type II superconductors. *Advances in Physics*, *21*(90), 199–428. https://doi.org/10.1080/00018737200101288

Gömöry, F. (1997). Characterization of high-temperature superconductors by AC susceptibility measurements. *Superconductor Science and Technology*, *10*(8), 523–542. https://doi.org/10.1088/0953-2048/10/8/001

Grilli, F., Pardo, E., Stenvall, A., Nguyen, D. N., Yuan, W., & Gömöry, F. (2014). Computation of losses in HTS under the action of varying magnetic fields and currents. *IEEE Transactions on Applied Superconductivity*, *24*(1), Article 8200433. https://doi.org/10.1109/TASC.2013.2259827

Gurevich, A., & Brandt, E. H. (1997). ac response of thin superconductors in the flux-creep regime. *Physical Review B*, *55*(18), 12706–12718. https://doi.org/10.1103/PhysRevB.55.12706

Hong, Y., Zheng, J., & Liao, H. (2019). Modeling of high-Tc superconducting bulk using different Jc–T relationships over dynamic permanent magnet guideway. *Materials*, *12*(18), Article 2915. https://doi.org/10.3390/ma12182915

Kim, Y. B., Hempstead, C. F., & Strnad, A. R. (1963). Magnetization and critical supercurrents. *Physical Review*, *129*(2), 528–535. https://doi.org/10.1103/PhysRev.129.528

Norris, W. T. (1970). Calculation of hysteresis losses in hard superconductors carrying ac: Isolated conductors and edges of thin sheets. *Journal of Physics D: Applied Physics*, *3*(4), 489–507. https://doi.org/10.1088/0022-3727/3/4/308

Prigozhin, L. (1996). The Bean model in superconductivity: Variational formulation and numerical solution. *Journal of Computational Physics*, *129*(1), 190–200. https://doi.org/10.1006/jcph.1996.0243

Shen, B., Grilli, F., & Coombs, T. (2020). Overview of H-formulation: A versatile tool for modeling electromagnetics in high-temperature superconductor applications. *IEEE Access*, *8*, 100403–100414. https://doi.org/10.1109/ACCESS.2020.2996177

Zeldov, E., Clem, J. R., McElfresh, M., & Darwin, M. (1994). Magnetization and transport currents in thin superconducting films. *Physical Review B*, *49*(14), 9802–9822. https://doi.org/10.1103/PhysRevB.49.9802

Zhang, M., & Coombs, T. A. (2012). 3D modeling of high-Tc superconductors by finite element software. *Superconductor Science and Technology*, *25*(1), Article 015009. https://doi.org/10.1088/0953-2048/25/1/015009

Zhao, Y.-F., & Zhou, Y.-H. (2011). AC susceptibility for superconducting slab with regions of different critical-current densities. *Cryogenics*, *51*(8), 417–419. https://doi.org/10.1016/j.cryogenics.2011.03.003.

Corresponding author: Naziha Nassar Aneizan
nazehanassar5@gmail.com
General Directorate of Education Salahaddin, Ministry of Education, Iraq.
© 2026. Faculty of Technology Education. ATBU Bauchi. All rights reserved